Building Objective 3D Fault Representations in Active Tectonic Settings

by Magali Riesner, Pauline Durand-Riard, Judith Hubbard, Andreas Plesch, and John H. Shaw

ABSTRACT

Developing 3D representations of active faults is an important step to improve seismic-hazard assessment. However, the geometries of faults can be difficult to constrain at depth, and building representations is often subjective. We present a new objective workflow to build 3D fault geometries from surface and subsurface data that are generally available in active tectonic environments. We use surface traces, focal mechanism orientations, and relocated hypocenters as geological constraints in an implicit modeling approach. This method enables us to control the weights assigned to the different constraints, increasing the accuracy of the fault model. We evaluate and refine our method by applying it to a well-known natural case study: the Puente Hills thrust fault, a blind thrust beneath Los Angeles, California, that is imaged by high-quality seismic reflection data and that generated the 1987 M_w 6.0 Whittier Narrows earthquake. Then, we apply our new workflow to the Xianshuihe–Anninghe left-lateral strike-slip fault systems, China. Implementing this workflow allows for the development of improved fault surface representations that can contribute to Community Fault Models and support fault system modeling, rupture simulations, and regional hazard assessments.

INTRODUCTION

Advances in theory and computing power allow the use of more complex 3D fault geometries in earthquake science. In particular, complex fault surface representations incorporated in modeling of fault system behavior (e.g., Marshall *et al.*, 2009; Herbert *et al.*, 2014; Thompson *et al.*, 2015, Hubbard *et al.*, 2016) and dynamic rupture simulations (Lozos *et al.*, 2015; Duru and Dunham, 2016) have shown that fault geometry plays a significant role in fault behavior throughout the earthquake cycle. Building more accurate 3D active fault representations is thus essential to improve seismic-hazard assessment. However, the geometries of faults can be difficult to constrain at depth in areas of limited data.

The most direct fault observations are outcrop measurements, surface traces, constraints from seismic reflection profiles, and fault cuts from well data. These data are regularly used to construct triangulated surface (t-surf) representations of the faults (e.g., Plesch *et al.*, 2007), because such surfaces can satisfy complex 3D spatial constraints. The available data are used to fit progressively a t-surf, and then the irregular surface is typically smoothed (Mallet, 2002; Caumon *et al.*, 2009).

Recent techniques have incorporated these earthquake data to help build 3D fault models (Carena and Suppe, 2002; Mallet, 2002; Shaw *et al.*, 2002; Carena *et al.*, 2004; Carena, 2007). These approaches have constrained fault surfaces by selecting points that illuminate the fault, such as clusters of earthquakes, fault traces, and seismic reflection profiles. Although integrating these data generally improves the resulting fault surface, it can be difficult to appropriately assign weights to the different geological constraints. For example, existing methods do not formally take into account the quality of the data, which can lead to inaccurate models; assigning lower weights to poor quality data would presumably improve model accuracy. In addition, these methods generally select earthquake clusters that might define a given fault manually, which can be highly subjective and a source of inaccuracy. Automated hypocenter selection would make this procedure reproducible and less subjective, helping to ensure that different faults within a region are represented consistently and that development of these surfaces can be reproduced. Another limitation with these current methods is that they do not generally use the focal mechanism information directly in fault construction, but rather for qualitative assessment of the generated surfaces, thus overlooking an important constraint on the fault orientation.

In the last few years, a new approach has been developed to build 3D geological horizons using sparse field data (Moyen *et al.*, 2004; Caumon *et al.*, 2007; Frank *et al.*, 2007; Calcagno *et al.*, 2008). Instead of directly constructing a surface honoring the available data, a scalar field is interpolated in a tetrahedral mesh using geological constraints. The surfaces are defined as isovalues ϕ of the stratigraphic property f (Moyen *et al.*, 2004; Caumon *et al.*, 2007, 2008, 2009; Frank *et al.*, 2007). To interpolate the scalar field, constraints on the location and orientation of the property can be used. Then, weights are assigned to these constraints according to the data type and quality.

Following this approach, we present a new, objective, and reproducible methodology for constructing 3D fault geometries using surface and subsurface constraints. We incorporate surface traces, focal mechanism orientations, and relocated

doi: 10.1785/0220160192

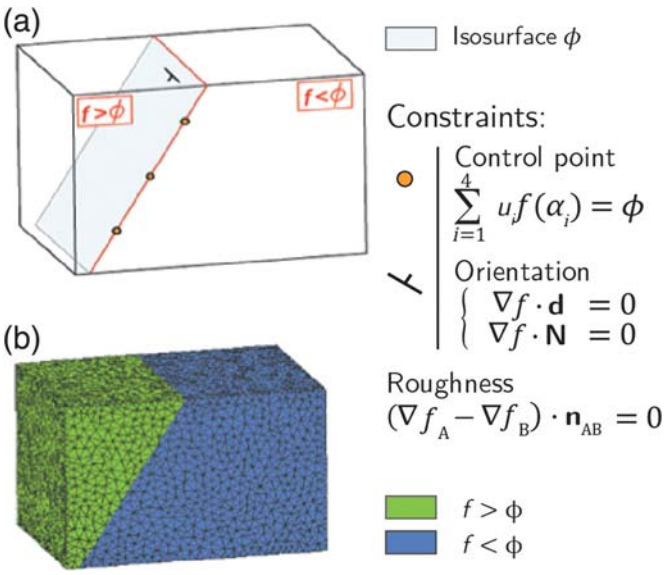

▲ **Figure 1.** (a) Constraints used to interpolate the fault property f on the tetrahedral mesh (in which u_i are the barycentric coordinates of the control point in the tetrahedra and α_i are the coordinates of the tetrahedra nodes. **N** and **d** are the strike and dip of the orientation constraint, respectively. (b) Resulting scalar field interpolated in a tetrahedral mesh. The fault surface corresponds to the value ϕ of the property f.

hypocenters in an iterative workflow, with steps along the way for the user to examine and assess the resulting surface.

We test this method by applying it to the Puente Hills thrust (PHT) fault, a blind thrust that lies beneath the city of Los Angeles, California (Shaw and Shearer, 1999; Shaw *et al.*, 2002). Industry seismic reflection data provide direct constraints on the subsurface structure of the PHT fault to depth of 7 km, while an earthquake with associated aftershocks provides constraints on the fault geometry at greater depths. We show that the fault surface produced using our method and the seismologic constraints closely fits the subsurface structure evident in the seismic reflection data. Then, we apply our method to a part of the Xianshuihe–Anninghe strike-slip fault system, China, to evaluate the method in a different tectonic environment with sparser data.

METHODOLOGY

Using the Implicit Approach for Surface Reconstruction

3D geological horizons were classically built as surfaces directly honoring the available data. However, recently a new approach to build 3D surfaces using sparse field data has been developed (Moyen *et al.*, 2004; Caumon *et al.*, 2007, 2008, 2009; Frank *et al.*, 2007; Calcagno *et al.*, 2008). In this implicit method, the geological constraints are used to interpolate a scalar field in a tetrahedral mesh. We propose in this article to follow this approach to build fault surfaces, incorporating field observations and earthquake data to constrain fault plane geometries. First, we generate a tetrahedral mesh, large enough to include all of the data. A property is interpolated based on the data such that the isovalue ϕ defines the fault surface, as described below (Fig. 1). Three types of constraints are used to interpolate this property:

- Hypocenter locations, fault traces, geological cross-section information, fault cuts from well data, and fault interpretations in seismic reflection profiles are assigned as control points, in which the value of the field is ϕ:

$$\sum_{i=1}^{4} u_i f(\alpha_i) = \phi, \tag{1}$$

  in which u_i are the barycentric coordinates of the control point in the tetrahedra, α_i are the coordinates of the tetrahedra nodes, and f is the value of the scalar field.
- Orientation constraints are derived from nodal planes of focal mechanisms at depth and from strike and dip measurements at any location, most commonly along the surface trace. An implicit fault surface honors this orientation information if the gradient of the scalar field at the orientation point is orthogonal to both strike (**N**) and dip (**d**) vectors:

$$\begin{cases} \nabla f \cdot \mathbf{d} = 0 \\ \nabla f \cdot \mathbf{N} = 0 \end{cases}, \tag{2}$$

  in which · stands for the dot product.
- In addition, to ensure the consistency of the interpolated property, a constant gradient constraint is added. This roughness constraint requires the gradient of the property to remain constant at the boundary between two adjacent tetras (A and B)

$$(\nabla f_A - \nabla f_B) \cdot \mathbf{n_{AB}} = 0 \tag{3}$$

  (Frank *et al.*, 2007), in which · stands for the dot product and $\mathbf{n_{AB}}$ is the normal vector to the face shared by tetras A and B.

We assign a weight to each of the constraints, which are defined manually (see discussion in the Resulting Fault Surface and Quality Control section).

Proposed Workflow

Our proposed workflow is presented in Figure 2a and includes two main components.

1. The initial surface (stage I surface) is interpolated from the orientation of the focal mechanism nodal planes and location data, such as the fault traces projected on a digital elevation model (DEM), seismic reflection data, and well cuts (where available).
2. Hypocenters are selected, involving two steps. First, an initial cluster is automatically selected according to a chosen distance between the stage I fault and the hypocenter location. This cluster is then added as control points when generating the stage II surface.

After these two calculations, we perform a third step to refine the cluster of hypocenters used to construct the fault. To do this, we generate a histogram of the distances between the fault surface and the hypocenter locations and identify modes (peaks). The mode closest to the stage II fault is considered to

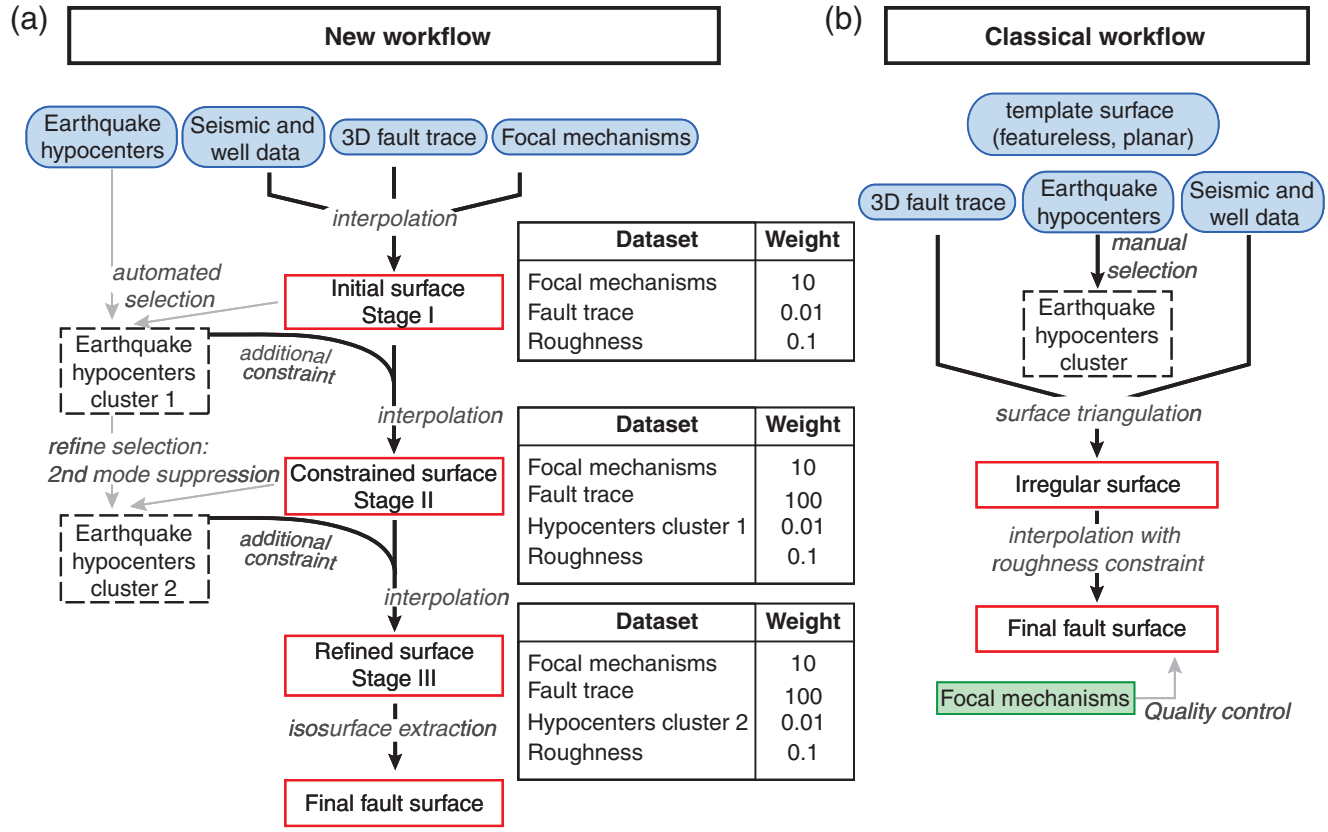

▲ **Figure 2.** (a) Classical 3D fault construction workflow of Carena and Suppe (2002) and Carena *et al.* (2004) as explained in the Introduction. (b) Our proposed workflow for 3D construction of fault surfaces.

represent hypocenters that illuminate the fault plane, whereas second or higher modes typically represent clusters associated with other faults. Thus, hypocenters beyond the minimum separating the primary and secondary modes are removed from the cluster. We do this by using this minimum as the new input distance to select hypocenters. The surface is then re-interpolated using the refined cluster and the other constraints. This yields a stage III surface that is unaffected by hypocenters that are considered not to illuminate the primary fault plane. If this changes the fault surface significantly, a fourth refinement step can be conducted to further refine the hypocenters.

The final surface can then be extrapolated or trimmed depending on the needs of the targeted modeling effort. In our case, we cut the upper border of the modeled surface with the fault trace projected on a DEM. To cut the base of the fault, we use a surface representing the base of the seismogenic part of the crust, which corresponds to the depth above which 99.9% of the moment release has occurred (Nazareth and Hauksson, 2004).

Compared with the classical approach (Fig. 2b), this new workflow enables us to use the focal mechanism nodal plane as a constraint to build the surface, rather than simply for quality control. Moreover, the cluster of hypocenters used to interpolate the final surface (stage III) is automatically selected and refined by a well-defined process, increasing the objectivity of the method.

TESTING THE PROCEDURE USING THE PHT, CALIFORNIA

Case Study Location and Dataset

We apply this workflow to a natural case study of the PHT system to evaluate and refine our method. This active thrust system underlies the high-rise district of Los Angeles, California, and thus represents a significant seismic hazard. The fault includes three en echelon north-dipping blind ramps that terminate upward at 2–3 km depth (Fig. 3; Shaw *et al.*, 2002). The middle thrust ramp, known as the Santa Fe Springs segment, produced an M_w 6.0 earthquake in 1987 (the Whittier Narrows earthquake), with associated aftershocks (Hauksson and Jones, 1989). This fault system provides high-quality data that can be used to apply our method: a surface trace, focal mechanisms, and aftershocks. Because the fault is blind, we use the top of the blind-thrust ramp, which has been mapped in seismic data, instead of a surface trace. In addition, high-quality industry seismic reflection data accurately image the geometry of the fault in the subsurface down to 7 km depth. These data will be used to evaluate our modeled fault surface.

Initial Surface Construction

The first step (stage I) is the construction of an initial fault surface. This surface uses two pieces of data as constraints: the surface trace of the fault (this provides a location) and any focal

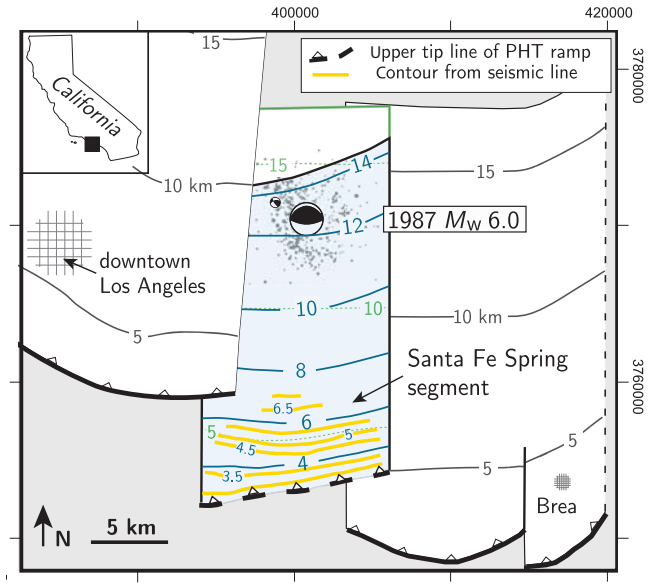

▲ **Figure 3.** Contour map of segments of the Puente Hills Thrust, showing the location of the 1987 Whittier Narrows earthquake sequence (Hauksson and Jones, 1989) relocated by Shaw and Shearer (1999) (UTM Zone 11, NAD27 datum). Santa Fe fault segment geometry modified after Shaw *et al.* (2002) in green, our modeled geometry in blue. Yellow contour lines represent interpretations from high-quality industry seismic reflection data that image the geometry of the fault down to 7 km depth.

mechanisms associated with the fault (this provides orientation information). This initial step is necessary, because it allows us to (1) distinguish between the principal and auxiliary nodal planes of the focal mechanisms; and (2) create the stage I surface (Fig. 4). For many faults, step (1) simply amounts to comparing the strikes of the nodal planes with the trend of the fault trace. However, for other faults, identifying the appropriate nodal plane may require examining aftershock distributions or *apriori* knowledge about the dip direction of the fault. When multiple focal mechanisms from different events are available, their influence on the different parts of the fault is weighted according to their locations. The weight attributed to the orientation constraint associated with each focal mechanism is greater closer to its location. Furthermore, we recommend selecting focal mechanisms with magnitudes that are appropriate for the fault being modeled. For example, events should be large enough to be confidently associated with the fault plane and not so large that they represent ruptures involving distinct faults or fault segments (multisegment ruptures). In case of multiple focal mechanism solutions for the same event, one might either choose to select one or all the solutions. However, this must be noted in the database catalog for reproducibility.

Selection of Hypocenters

The selection of hypocenters is a process evolving through stages I–III. After the initial surface construction, we use the initial fault surface (constrained only with the fault trace and the focal mechanisms) to automatically select a set of hypocenters that are associated with the fault. All hypocenters within a specified distance of the stage I fault are included. We include earthquakes within 10 km (Fig. 5a) and recommend that this choice should be made to ensure that all earthquakes potentially associated with the fault are included in this first step. The hypocenters are then added as constraints to generate the stage I fault and refine the fault model.

In the second step (stage II), we use the stage I fault surface to refine the selected hypocenters and find the appropriate cluster associated with the fault. This step is performed by considering the histogram of the distance between the stage I fault and the hypocenter locations. In this case, a cluster of hypocenters is observable within a distance of 6.5 km from the fault. We create a new cluster including only the hypocenters within 6.5 km from the stage I fault. Then, this new cluster is added as constraints to generate the stage II fault, thus replacing the first cluster including hypocenters within 10 km of the fault.

Once the stage II fault is generated, we perform a control step to assess the need to refine the hypocenter cluster. The histogram of the distance between the stage II fault and the hypocenter locations shows a second mode at ~3.2 km (Fig. 5b). We create a refined cluster using the minimum between first and second modes (3.1 km) as a new distance threshold, thus removing second and higher modes. A comparison of the stage II surface with the hypocenters showed that a cluster of events was located in the hanging wall of the fault surface associated with the largest aftershock (M_w 5.3). This event had a strike-slip mechanism (Hauksson and Jones, 1989) and is associated with a splay of the Whittier fault (Shaw *et al.*, 2002). It, therefore, does not provide a direct constraint on the shape of the PHT fault. We eliminate this local hypocenter cluster from the constraints used to model the PHT fault, yielding a stage III fault that is more consistent with direct constraints on the fault surface.

Resulting Fault Surface and Quality Control

The resulting fault surface, using the new refined earthquake cluster, is shown in Figure 5a. Because the PHT fault is blind, the upper border of the fault surface is here delimited by the top of the blind-thrust ramp, mapped in seismic data. The base of the fault is defined by the seismogenic thickness of the California crust (Nazareth and Hauksson, 2004).

To assess the accuracy of our approach, we compare our final surface with high-quality industry seismic reflection data that clearly image the PHT fault down to 7 km (Figs. 3 and 5). The modeled fault surface closely fits the geometry interpreted from the seismic reflection lines, with the standard deviation of the modeled and interpreted fault being only 72 m. This test case demonstrates that the methodology that we have developed is an effective way of modeling 3D fault surfaces. Naturally, to obtain a better final fault representation one should add the seismic reflection data as control points for the fault location. Several tests have been performed using different weights for the constraints, and the results shown here yield the best match with the independently interpreted fault surface. Below, we further evaluate the weighting of these constraints in our application

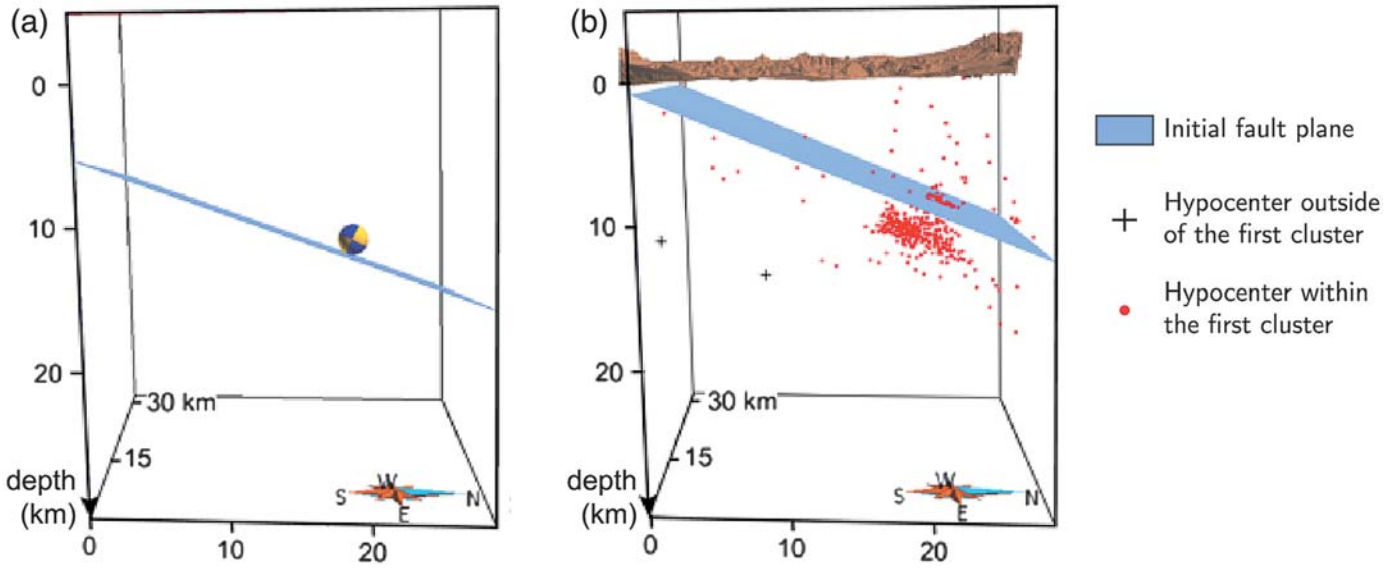

▲ **Figure 4.** (a) Selection of the principal nodal plane of the 1987 Whittier Narrows (M_w 6) earthquake. Focal mechanism from Hauksson and Jones (1989). (b) Cluster of hypocenters within 10 km of the initial fault plane (stage I: the initial fault plane is built using only the orientation from the nodal plane and the location of the fault trace, then the first cluster of hypocenter is automatically selected); topography is also shown.

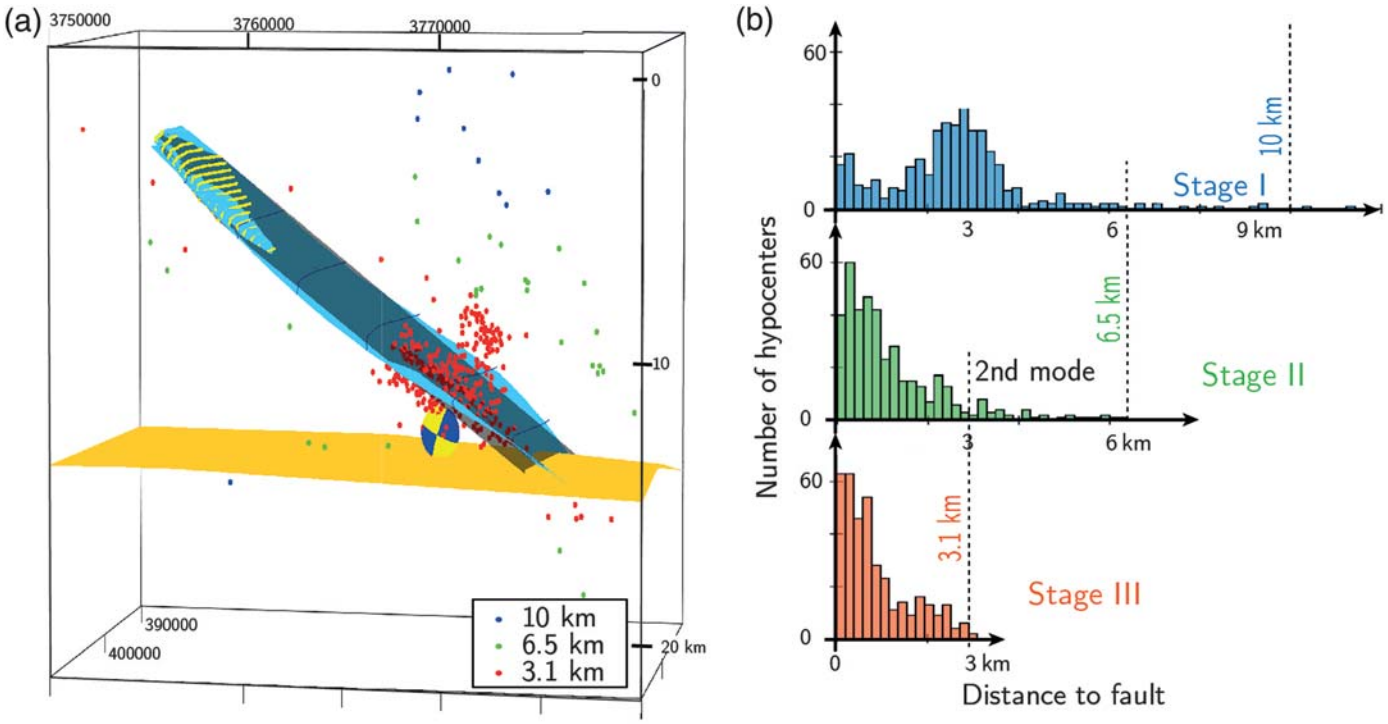

▲ **Figure 5.** (a) Perspective view of final surface (light blue) of the Santa Fe fault showing the location of the 1987 Whittier Narrows earthquake sequence (Hauksson and Jones, 1989) relocated by Shaw and Shearer (1999). The California Community Fault Model surface (Plesch *et al.*, 2007) is shown in transparent dark blue surface for comparison. Yellow contour lines represent interpretations from high-quality industry seismic reflection data that image the geometry of the fault down to 7 km depth. Hypocenters used in each step are represented. Orange surface represents the base of the seismogenic crust. (b) Hypocentral distribution relative to modeled fault at the different stages and cluster threshold for next stage of modeling.

to fault systems in China and subsequently provide recommendations for their use in other applications.

Our fault representation is very similar to the one included in the California Community Fault Model (Plesch *et al.*, 2007; see Fig. 5). However, the California Community Fault Model is a fault-focused approach, with hypocenter clusters used on a case-by-case basis, as compared to our more quantitative workflow approach.

APPLICATION TO PART OF THE XIANSHUIHE–ANNINGHE FAULT SYSTEM IN CHINA

Geological Setting

The 2008 M_w 7.9 Wenchuan earthquake struck the Sichuan province of central China, along the Longmen Shan fold-and-thrust belt, at the eastern margin of the Tibetan plateau (Burchfiel *et al.*, 2008; Stone, 2008). The rupture occurred in a region with no prior historic earthquakes of comparable size and with only modest amounts of horizontal shortening (Chen *et al.*, 2000; Shen *et al.*, 2005). Therefore, the event occurred with little prior warning based on current methods of seismic-hazard assessment.

East of this complex Longmen Shan system that ruptured during this earthquake (Hubbard and Shaw, 2009; Hubbard *et al.*, 2010) northwest–southeast-striking strike-slip systems accommodate the extrusion of the Tibetan plateau away from the Himalayan collision zone: the Xianshuihe–Anninghe fault system to the southwest and the Kunlun fault to the northeast. These faults have produced M_w 7 earthquakes in recorded history and have high slip rates (6–12 mm/yr) (Wen, Fan, *et al.*, 2008).

As part of an ongoing effort to produce a Sichuan–Longmen Shan Community Fault Model (Hubbard *et al.*, 2012), we select the Xianshuihe–Anninghe fault system for a second case study to apply and test our method, given the natural complexity of the fault system and the availability of seismologic and geologic data.

Dataset

We apply our workflow to define the 3D geometries of the Xianshuihe and Anninghe faults. To build a well-constrained model, we use data from a variety of sources (Fig. 6).

- Fault traces based on maps from the Chinese Geological Survey, with additional detailed traces from regional and local studies (Allen *et al.*, 1991; He *et al.*, 2008).
- Focal mechanisms from the Global Centroid Moment Tensor project (see Data and Resources) and regional studies (Allen *et al.*, 1991; Papadimitriou *et al.*, 2004).
- A dataset of seismicity (1970–2011) was constructed from a combination of relocated seismicity (1992–2002) provided by Zhu *et al.* (2005) and the Wenchuan aftershocks (2008–2009), supplemented with less precisely located seismicity from the China Seismic Network for the missing time periods (see Data and Resources).

Following the method of Nazareth and Hauksson (2004), we constructed a surface representing the base of the seismogenic part of the crust.

The Xianshuihe and Anninghe faults comprise a left-lateral strike-slip system that is at least 1400 km long. The

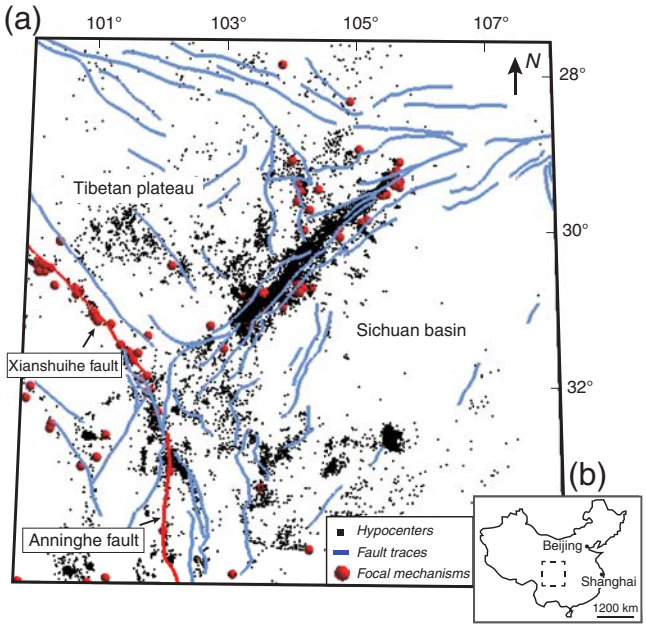

▲ **Figure 6.** (a) Fault map, focal mechanisms from Generic Mapping Tool (GMT) catalog, Allen *et al.* (1991), Kirby *et al.* (2000), Papadimitriou *et al.* (2004), Yang *et al.* (2005), Wen, Fan, *et al.* (2008), and hypocenters' location from China Seismologic Network and Zhu *et al.* (2005) catalog used for the fault modeling. (b) Location of the map within China.

Xianshuihe fault strikes N40°W, with an average slip rate of 10 ± 2 mm/yr. The fault has produced four $M_w \geq 7$ earthquakes along its 350-km length during the last century (Allen *et al.*, 1991). Furthermore, Allen *et al.* (1991), Wen, Fan, *et al.* (2008), and Wen, Ma, *et al.* (2008) suggest that 18 $M_w \geq 6$ earthquakes occurred on this structure from the fourteenth century to 1981. These include major earthquakes in 1904 (M_w 7.0), 1923 (M_w 7.5), 1973 (M_w 7.6), and 1981 (M_w 6.9), which occurred on the 150-km-long fault segment including Luhuo and Daofu with overlapping fault ruptures and with individual left-lateral displacement up to 3.6 m.

At the southern end of the Xianshuihe fault, the Anninghe fault strikes north–south. Two large earthquakes occurred in this region, in 1913 (M_w 6) and 1952 (M_w 6.75). From 1970 to 1977, three $4 \leq M_w \leq 5.3$ events occurred along the fault. However, since January 1977, the Anninghe fault has experienced a 30-year period of seismic quiescence, with no earthquakes of $M_w \geq 4$ (Wen, Fan, *et al.*, 2008).

Modeling the Fault Surfaces

Both the Xianshuihe and Anninghe faults have well-mapped surface traces. The Xianshuihe fault is also defined by seismicity that lies roughly beneath the fault trace and by a set of 15 focal mechanisms. These mechanisms show left-lateral motion, with the principal nodal plane striking parallel to the fault trace and having a nearly vertical dip (73°–90°) (Fig. 7a). The Anninghe fault shows significant seismicity at its northern tip but is less well defined to the south. Only two focal mechanisms are available to constrain its dip. These focal mechanisms, along

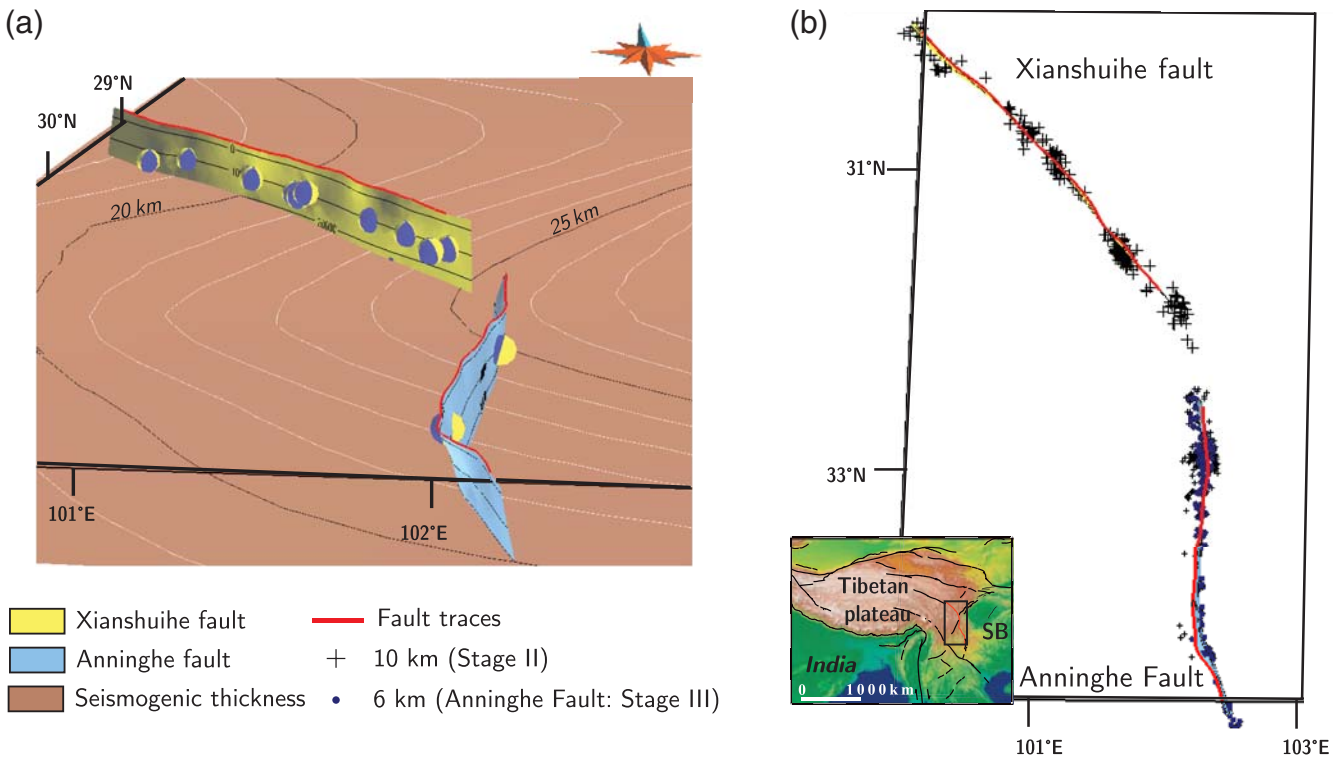

▲ **Figure 7.** (a) Map view of the Xianshuihe and Anninghe fault surfaces with the different clusters of hypocenters used in the modeling (hypocenter locations from the China Seismologic Network and Zhu *et al.*, 2005). (b) 3D view of the modeled faults showing the focal mechanisms used as constraints (focal mechanisms from GMT catalog, Allen *et al.*, 1991; Papadimitriou *et al.*, 2004; Yang *et al.*, 2005; Wen *et al.*, 2008; and Kirby *et al.*, 2000). Plunges represent the hypocenter clusters used to constraint the stage II faults and in the Anninghe case; dots are used for the stage III faults. SB, Sichuan basin.

with the hypocenter locations, are also consistent with a nearly vertical fault (75° dip)

We use these data to apply our workflow. We perform stage I modeling using only the fault traces and focal mechanisms. Then, we use a default distance of 10 km to select our initial set of hypocenters for stage II modeling. Figure 7b shows the locations of hypocenters used in the stage II fault model. In both cases, the stage II model seems to fit the hypocenters well, with most of the hypocenters very close to the fault. A second mode can be identified in the Anninghe distribution of hypocenters relative to the stage II fault model at about 7 km from the fault (see Fig. 8). This second mode is likely due to seismicity on the set of faults that splay off from the northern tip of the Anninghe fault. To remove these distant hypocenters from our modeling constraints, we cut off the seismicity at 6 km rather than 10 km to define a stage III Anninghe fault model. The new hypocentral cluster is shown in Figure 7b. No such second mode is visible for the Xianshuihe fault; we therefore keep the stage II model for this fault.

We cut both of these faults by topography and a surface that represents the base of seismicity to define their vertical limits. An analysis of the stage III surface shows that it varies smoothly in 3D, with local strike and dip orientations that are consistent with all of the available geologic and seismologic data. This implies that they are viable representations of the fault surfaces.

The weighting of constraints that we used for these faults was the same as that used for the PHT fault. This suggests that similar weightings can be used for faults in different regions and tectonic environments. However, it may be useful to consider different weighting constraints in applications in which uncertainties in the data types vary. Furthermore, weights are assigned per hypocenters, thus it is often necessary to scale the weighting of the cluster by the number of hypocenters. To assess the uncertainties in these fault representations and the possibility of alternative representations, one might test a wide range of weighting parameters and compare the results with data that were not included in the initial analysis. We noticed that a small variation in the parameters weighting (less than half-order of magnitude for the focal mechanism and the fault trace and less than one order of magnitude for the hypocenter cluster) affect the fault representation by a few tenths of meters only. However, any larger variations result in an unrealistic fault representation. Moreover, as additional seismologic and geologic data become available, our modeling approach provides a way to objectively incorporate these new constraints in a revised version of the fault surface. For example, in case of detectable surface deformation associated with moderate-to-large earthquakes, Global Positioning System and Interferometric Synthetic Aperture Radar-derived fault geometry can be incorporated as new control points constraining the fault

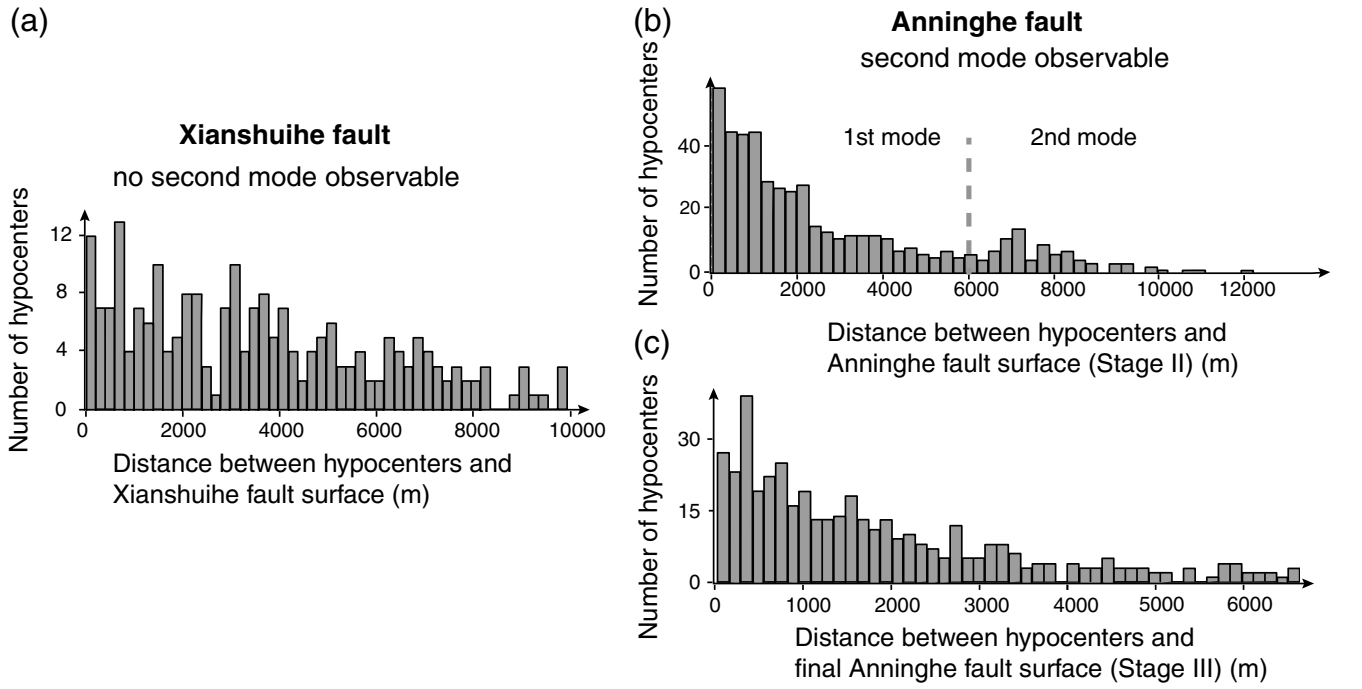

▲ **Figure 8.** Hypocentral distribution at the different stages, and cluster threshold for next stage modeling. (a) Distance from stage II modeled Xianshuihe fault. No second mode is observable. (b) Distance from stage II modeled Anninghe fault; two modes are observable. (c) Distance from stage III modeled Anninghe fault produced after removal of the second mode.

location. Furthermore, as proposed for the California Community Fault Model (Plesch *et al.*, 2007), alternative representations can be produced for a given fault involving different levels of details by selecting different constraints.

CONCLUSIONS

We developed a new objective workflow to define 3D geometries of strike-slip, oblique-slip, and dip-slip faults. The method uses the implicit modeling approach (Moyen *et al.*, 2004; Caumon *et al.*, 2007; Frank *et al.*, 2007; Calcagno *et al.*, 2008) and is flexible, accommodating a variety of datasets, such as surface traces, seismicity, cross sections, fault cuts, focal mechanism orientations, and faults interpreted from seismic reflection data. These datasets can be weighted by the user according to their quality.

We validated the methodology by applying it to the Santa Fe Springs segment of the PHT, California. We used the mapped top of the blind-thrust ramp combined with seismicity and the nodal plane of a focal mechanism to develop a 3D model of the thrust. We show that this model closely matches the fault geometry interpreted from seismic reflection data.

Then, we applied the workflow to two strike-slip faults in Sichuan province, China: the Xianshuihe and Anninghe faults. Here, we used the mapped surface traces, large seismicity datasets, and focal mechanisms to generate 3D fault models. The resulting faults dip steeply and show local variations and undulations that fit the subsurface data. This approach can be implemented to develop realistic 3D fault surfaces in various active tectonic setting to support the development of Community Fault Models and other applications.

DATA AND RESOURCES

The Global Centroid Moment Tensor project database was searched using http://www.globalcmt.org/CMTsearch.html (last accessed December 2011) and the China Seismic Network using http://www.csndmc.ac.cn/wdc4seis@bj/earthquakes/csn_catalog_p001.jsp (last accessed December 2011).

ACKNOWLEDGMENTS

The authors thank the Harvard China Fund for helping to facilitate this research. The research used software (Gocad) generously granted to Harvard University by Paradigm. We also thank Landmark Graphic Corporation for providing software used to analyze geophysical data in this study through their University Grant Program.

REFERENCES

Allen, C. R., L. Zhuoli, Q. Hong, W. Xueze, Z. Huawei, and H. Weishi (1991). Field study of a highly active fault zone: The Xianshuihe fault of southwestern China, *Geol. Soc. Am. Bull.* **103,** no. 9, 1178–1199.

Burchfiel, B. C., L. H. Royden, R. D. van der Hilst, E. H. Hager, Z. Chen, R. W. King, C. Li, J. Lü, H. Yao, and E. Kirby (2008). A geological and geophysical context for the Wenchuan earthquake of 12 May 2008, Sichuan, People's Republic of China, *GSA Today* **18,** no. 7.

Calcagno, P., J.-P. Chilès, G. Courrioux, and A. Guillen (2008). Geological modelling from field data and geological knowledge Part I. Modelling method coupling 3D potential-field interpolation and geological rules, *Phys. Earth Planet. In.* **171,** nos. 1/4, 147–157.

Carena, S. (2007). Using earthquake data to map faults in 3-D with Gocad: Examples at different scales, *Wissenschaftliche Mitteilungen* **35,** 193–200.

Carena, S., and J. Suppe (2002). Three-dimensional imaging of active structures using earthquake aftershocks: The Northridge thrust, California, *J. Struct. Geol.* **24,** no. 4, 887–904.
Carena, S., J. Suppe, and H. Kao (2004). Lack of continuity of the San Andreas Fault in southern California: Three-dimensional fault models and earthquake scenarios, *J. Geophys. Res.* **109,** doi: 10.1029/2003JB002643.
Caumon, G., C. Antoine, C. le Carlier de Veslud, M.-O. Titeux, G. Gray, J. Pellerin, C. Castagnac, N. Cherpeau, C. Cavelius, F. Lallier, *et al.* (2008). Implicit 3D model building from remote sensing and sparse field data—Application to La Popa Basin, Mexico, *Proc. of the 28th Gocad Meeting*, Nancy, France.
Caumon, G., C. Antoine, and A.-L. Tertois (2007). Building 3D geological surfaces from field data using implicit surfaces, *Proc. Gocad Meeting*, Nancy, France, 1–6.
Caumon, G., P. Collon-Drouaillet, C. Le Carlier de Veslud, J. Sausse, and S. Viseur (2009). Surface-based 3D modeling of geological structures, *Math. Geosci.* **41,** no. 9, 927–945.
Chen, Z., B. C. Burchfiel, Y. Liu, R. W. King, L. H. Royden, W. Tang, E. Wang, J. Zhao, and X. Zhang (2000). Global Positioning System measurements from eastern Tibet and their implications for India/Eurasia intercontinental deformation, *J. Geophys. Res.* **105,** no. 16, 16,215–16,227.
Duru, K., and E. M. Dunham (2016). Dynamic earthquake rupture simulations on nonplanar faults embedded in 3D geometrically complex, heterogeneous elastic solids, *J. Comput. Phys.* **305,** 185–207.
Frank, T., A.-L. Tertois, and J.-L. Mallet (2007). 3D reconstruction of complex geological interfaces from irregularly distributed and noisy point data, *Comput. Geosci.* **33,** no. 7, 932–943.
Hauksson, E., and L. Jones (1989). The 1987 Whittier Narrows earthquake sequence in Los Angeles, southern California: Seismological and tectonic analysis, *J. Geophys. Res.* **94,** no. B7, 940–960.
He, H., Y. Ikeda, Y. He, M. Togo, J. Chen, C. Chen, M. Tajikara, T. Echigo, and S. Okada (2008). Newly-generated Daliangshan fault zone—Shortcutting on the central section of Xianshuihe-Xiaojiang fault system, *Sci. China Earth Sci.* **51,** 1248–1258.
Herbert, J. W., M. L. Cooke, and S. T. Marshall (2014). Influence of fault connectivity on slip rates in southern California: Potential impact on discrepancies between geodetic derived and geologic slip rates, *J. Geophys. Res.* **119,** doi: 10.1002/2013JB010472.
Hubbard, J., and J. H. Shaw (2009). Uplift of the Longmen Shan and Tibetan plateau, and the 2008 Wenchuan (M 7.9) earthquake, *Nature* **458,** no. 1, 194–197.
Hubbard, J., R. Almeida, A. Foster, S. Sapkota, P. Burgi, and P. Taponnier (2016). Structural segmentation controlled the 2015 M_w 7.8 Gorkha earthquake rupture in Nepal, *Geology* **44,** doi: 10.1130/G38077.1.
Hubbard, J., J. H. Shaw, and Y. Klinger (2010). Structural setting of the 2008 M_w 7.9 Wenchuan earthquake, China, *Bull. Seismol. Soc. Am.* **100,** no. 5B, 2713–2735.
Hubbard, J., J. H. Shaw, A. Plesch, M. Riesner, H. Smith, M. Wang, and P. Durand-Riard (2012). A Community Fault Model (CFM) for the Sichuan basin and Longmen Shan, presented at *2012 Fall Meeting, AGU*, San Francisco, California, 3–7 December, Abstract T51G–08.
Kirby, E., K. X. Whipple, B. C. Burchfiel, W. Tang, G. Berger, Z. Sun, and Z. Chen (2000). Neotectonics of the Min Shan, China: Implications for mechanisms driving Quaternary deformation along the eastern margin of the Tibetan plateau, *Geol. Soc. Am. Bull.* **112,** no. 3, 375–393.
Lozos, J. C., D. D. Oglesby, J. N. Brune, and K. B. Olsen (2015). Rupture and ground motion models on the northern San Jacinto fault, incorporating realistic complexity, *Bull. Seismol. Soc. Am.* **105,** doi: 10.1785/0120140327.
Mallet, J.-L. (2002). *Geomodeling*, Oxford University Press, New York, New York, 624 p.
Marshall, S. T., M. L. Cooke, and S. E. Owen (2009). Interseismic deformation associated with three-dimensional faults in the greater Los Angeles region, California, *J. Geophys. Res.* **114,** no. B12403, doi: 10.1029/2009JB006439.
Moyen, R., J.-L. Mallet, T. Frank, B. Leflon, and J.-J. Royer (2004). 3D-parameterization of the 3D geological space—The GeoChron model, *Proc. European Conference on the Mathematics of Oil Recovery IX*, Cannes, France, 8 p.
Nazareth, J. J., and E. Hauksson (2004). The seismogenic thickness of the southern California crust, *Bull. Seismol. Soc. Am.* **94,** no. 3, 940–960.
Papadimitriou, E., X. Wen, V. Karakostas, and X. Jin (2004). Earthquake triggering along the Xianshuihe fault zone of western Sichuan, China, *Pure Appl. Geophys.* **161,** 1683–1707.
Plesch, A., J. H. Shaw, C. Benson, W. A. Bryant, S. Carena, M. Cooke, J. Dolan, G. Fuis, E. Gath, L. Grant, *et al.* (2007). Community fault model (CFM) for Southern California, *Bull. Seismol. Soc. Am.* **97,** 1793–1820, doi: 10.1785/0120050211.
Shaw, J. H., and P. M. Shearer (1999). An elusive blind-thrust fault beneath metropolitan Los Angeles, *Science* **283,** no. 5407, 1516–1518.
Shaw, J. H., A. Plesch, J. F. Dolan, T. L. Pratt, and P. Fiore (2002). Puente Hills blind-thrust system, Los Angeles, California, *Bull. Seismol. Soc. Am.* **92,** no. 8, 2946–2960.
Shen, Z. K., J. N. Lu, M. Wang, and R. Burgmann (2005). Contemporary crustal deformation around the southeast borderland of the Tibetan plateau, *J. Geophys. Res.* **110,** doi: 10.1029/2004JB003421.
Stone, R. (2008). Geophysics: An unpredictably violent fault, *Science* **320,** 1578–1580.
Thompson, T. B., A. Plesch, J. H. Shaw, and B. J. Meade (2015). Rapid slip-deficit rates at the eastern margin of the Tibetan plateau prior to the 2008 M_w 7.9 Wenchuan earthquake, *Geophys. Res. Lett.* **42,** no. 6, 1677–1684.
Wen, X., J. Fan, G. Yi, Y. Deng, and F. Long (2008). A seismic gap on the Anninghe fault in western Sichuan, China, *Sci. China Earth Sci.* **51,** 1375–1387, ISSN 1006–9313.
Wen, X., S.-L. Ma, X. Xi-wei, and H. Yong-nian (2008). Historical pattern and behavior of earthquake ruptures along the eastern boundary of the Sichuan-Yunnan faulted-block, southwestern China, *Phys. Earth Planet. In.* **168,** nos. 1/2, 16–36.
Yang, Z. X., F. Waldhauser, Y. T. Chen, and P. G. Richards (2005). Double-difference relocation of earthquakes in central-western China, 1992–1999, *J. Seismol.* **9,** 241–264.
Zhu, A.-L., X.-W. Xu, Y.-S. Zhou, J.-Y. Yin, W.-J. Gan, and G.-H. Chen (2005). Relocation of small earthquakes in western Sichuan, China and its implications for active tectonics, *Chin. J. Geophys.* **48,** no. 3, 629–636.

Magali Riesner[1]
Pauline Durand-Riard[2]
Judith Hubbard[3]
Andreas Plesch
John H. Shaw
Department of Earth & Planetary Sciences
Harvard University
20 Oxford Street
Cambridge, Massachusetts 02138 U.S.A.
pauline.durandriard@gmail.com
judith.a.hubbard@gmail.com
andreas_plesch@harvard.edu
shaw@eps.harvard.edu

Published Online 1 March 2017

[1] Now at Département de Tectonique et mécanique de la lithosphère Institut de physique du globe, 1 rue jussieu, 75005 Paris; riesner@ipgp.fr.
[2] Now at Total S.A., CSTJF, Avenue Larribau, 64000, Pau, France.
[3] Now at Earth Observatory of Singapore, 50 Nanyang Avenue, Nanyang Technological University, 639798 Singapore.